IOWA STATE UNIVERSITY
Digital Repository

2020

Surface textures for stretchable capacitive strain sensors

Han Liu
Iowa State University

Surface textures for stretchable capacitive strain sensors

by

Han Liu

A thesis submitted to the graduate faculty

in partial fulfillment of the requirements for the degree of

MASTER OF SCIENCE

Major: Civil Engineering (Structural Engineering; Intelligent Infrastructure Engineering)

Program of Study Committee:
Simon Laflamme, Major Professor
Jiehua Shen
Eric Zellner
Derrick Rollins

The student author, whose presentation of the scholarship herein was approved by the program of study committee, is solely responsible for the content of this thesis. The Graduate College will ensure this thesis is globally accessible and will not permit alterations after a degree is conferred.

Iowa State University

Ames, Iowa

2020

TABLE OF CONTENTS

LIST OF TABLES

LIST OF FIGURES

ACKNOWLEDGMENTS

I would like to take this opportunity to express my thanks to those who helped me with various aspects of conducting research and the writing of this thesis.

First and foremost, Dr. Simon Laflamme for his guidance, patience and support throughout this research and the writing of this thesis. His insights and words of encouragement have often inspired me and renewed my hopes for completing my graduate education.

I would like to thank Dr. Matthias Kollosche and my colleague Jin Yan for their guidance throughout the initial stages of my graduate career. I would additionally like to thank Dr. Joseph A. Schaefer from the Department of Aerospace Engineering and Dr. Sarah A. Bentil from Department of Mechanical Engineering at Iowa State University for the assistance with the experiments.

I would also like to thank my committee members for their efforts and contributions to this work: Dr. Jiehua Shen, Dr. Eric Zellner, and Dr. Derrick K. Rollins.

Lastly, I would like to acknowledge the financial support of Iowa State University and the University of Iowa through the joint seed grant program. Also, the Ji'nan Huayuxin Casting Materials Co., Ltd. (Shandong, China) for providing the molds fabrication.

ABSTRACT

Advances in smart materials and electronics have enabled compliant sensing systems mimicking nature. In structural health monitoring (SHM) applications, the technology still lacks accuracy in tracking measurements over large geometries. Herein we report a facile fabrication for a compliant sensor based on an elastomeric capacitive sensor technology, augmented with a scalable surface texture inspired by various grid geometries. Texture designs are selected to direct, and therefore improve, the strain sensing capabilities and thus the sensor's gauge factor. We showcase selected designs based on an a detailed engineering analysis. The selected surface patterns are investigated under increasing strain targets and strain frequency sweeps. Results confirm that a stretchable thermoplastic composite sensor with a textured pattern embossed into the hyper-elastic matrix yields approximately 30% increase in the gauge factor and 35% in signal accuracy, great linearity up to 30% strain, and overall signal stability to empower SHM applications.

Keywords: sensor, composite, stretchable electronics, soft elastomeric capacitor, strain monitoring, structural health monitoring, dielectric polymer, texture, sensing skin.

CHAPTER 1.   GENERAL INTRODUCTION

The deployment of cost-effective solutions capable of monitoring very large surfaces is a key challenge in structural health monitoring (SHM). Recent advances in hyper-elastic materials and self-sensing sensor designs have enabled dense compliant sensor networks for the cost-effective monitoring of large-scale structures in science and engineering fields. The idea of a dense sensor network composed of sensing skins has attracted significant attention in the SHM community recently. These dense sensor networks are typically made of soft and flexible sensors in a dense network configuration, capable of measuring states discretely over a large surface. The authors have previously proposed and characterized a sensing skin based on soft polymer composites by developing soft elastomeric capacitor (SEC) technology that transduces any geometric variation into an electronically measurable change in capacitance. A limitation of the technology is in its low gauge factor and lack of sensing directionality that restricts area-wide signal reconstruction capabilities and requires the decomposition of the signal. In this paper, the SEC is stretchable in one direction only due to surface textures, which provide improvements in its performance by significantly decreasing its transverse Poisson's ratio, and thus improving its sensing directionality and gauge factor.

CHAPTER 2. SURFACE TEXTURES FOR STRETCHABLE CAPACITIVE STRAIN SENSORS

The content of this thesis has been submitted to *Smart Materials and Structures-IOPscience* Liu et al. (2020)

2.1 Background

Recent advances in self-sensing materials have enabled sensing skins for the cost-effective monitoring of large-scale structures. The authors have proposed sensing skin based on soft elastomeric capacitor (SEC) technology that transduces strain into a measurable change in capacitance. A limitation of the technology is in its low gauge factor and lack of sensing directionality. In this paper, we investigate the use of textures to improve on the SEC performance by significantly decreasing its transverse Poisson's ratio, and thus improving its sensing directionality and gauge factor. In particular, we investigate patterns inspired by transverse reinforcement. A numerical model is constructed and validated to numerically evaluate the performance of each pattern. Results show a significant improvement in sensing directionality, stability, and linearity.

Advances in soft complaint materials have significantly impacted science and engineering, including the fields of electronics Rogers et al. (2010); Wang et al. (2018), robotics Shepherd et al. (2011); Ilievski et al. (2011), and medicine Tybrandt et al. (2018). Of interest to this paper is the use of soft stretchable materials for structural health monitoring (SHM) applications to design a compliant, dense sensor networks with significantly improved adaptability compared with conventional sensors Mohammad and Huang (2010). Such dense sensor net-

works, termed sensing skins, aim to mimic biological skin and could provide unprecedented coverage and resolution in terms of state measurement capabilities.

Various sensors fabricated from flexible electronics have been proposed and studied for SHM applications Liao et al. (2015). The most common types are resistance-based and capacitance-based sensors Laflamme and Ubertini (2019). For instance, flexible resistance-based sensors have been developed using carbon nanotubes Srivastava et al. (2011) and graphene nanosheets Manna et al. (2019). Capacitance-based sensors have been proposed from bio-compatible polymers Burton et al. (2019) and nanocomposite thin films Lee et al. (2016). Research examples targeting biological skin mimicry for SHM applications include strain sensing sheets based on large area electronics and integrated circuits Tung et al. (2014); Zhang et al. (2014); Zhou et al. (2010), electrical impedance tomography Hallaji et al. (2014); Gupta et al. (2016), and multifunctional materials Downey et al. (2018); Yan et al. (2019).

2.1.1 Investigation

The authors have previously studied a sensing skin based on soft elastomeric capacitors (SEC) that transduces strain into a measurable change of capacitance Laflamme et al. (2013b). The SEC is fabricated from a thermoplastic elastomer mixed with rutile titanium dioxide and sandwiched between conductive composite layers made from the identical elastomer. The sensor technology has been demonstrated in a dense network configuration to measure strain fields on wind turbine blades Downey et al. (2017), and localize and quantify fatigue cracks on steel components Kong et al. (2016). However, a challenge in the deployment of the SEC technology is in its relatively low gauge factor and its lack of its intrinsic directional sensing capability that requires signal separation to obtain strain measurements along principal axes Downey et al. (2016).

The challenge of a directional sensing using soft thin-film sensors is however not new. To overcome technical limitations, recent studies in the field of soft robotics have proposed

a woven mesh Chou and Hannaford (1996) and rigid compartments Martinez et al. (2012); Tolley et al. (2014) acting as strain-limits for more predictable extension, twisting, and bending Deimel and Brock (2015). Such programmed directionality requires tedious fabrication, which is difficult to integrate into 2D geometries or into any scalable processes for flexible sensors, especially for SHM applications. Addressing the challenges of directional sensing, strain sensitivity, and scalability has the promise to empower thin-film sensors arrays to monitor large structures, such as transportation infrastructures and energy systems, providing rich high-resolution data that could be harnessed for condition-based maintenance decisions.

Previous studies published by the authors have shown that the sensitivity of a pristine SEC (i.e., no surface corrugation) depends on the dielectric permittivity Kollosche et al. (2011) and can be enhanced on the molecular level, and that its gauge factor is as a function of the apparent Poisson's ratios of the film and material/structure onto which the sensor is adhered Laflamme et al. (2013b) (note that unless specified otherwise, the Poisson's ratio discussed in this paper refers to the apparent Poisson's ratio of the SEC). For a pristine SEC, a lower Poisson's ratio leads to a higher gauge factor Laflamme et al. (2013b). Adjusting the Poisson's ratio has been widely employed recently to improve the gauge factor of flexible sensors Shintake et al. (2019); Li et al. (2016). Ameliorating the directionality of measurements of the SEC for SHM has not been addressed previously. In this paper, a surface textured SEC is proposed, with the objective of providing the sensor with higher sensitivity and sensing directionality. This is done by providing axial reinforcement patterns based on various grid geometries. The higher stiffness in the transverse direction leads to lower Poisson's ratio and minimizes the variation of capacitance induced by the transverse strain.

2.1.2 Paper Organization

This paper is organized as follows.

- **Section 2.1** Background: provides background information for the problems that the research is investigating and presents the objectives of the study.

- **Section 2.2** Design and fabrication of textured SEC: introduces the design and fabrication process of the textured sensors, and includes a derivation of the electromechanical model.

- **Section 2.3** Methodology: describes the methodology used to conduct the numerical study and experimental tests.

- **Section 2.4** Results and Discussion: presents numerical mode validation, numerical study, and Quasi-static test.

- **Section 2.5** Dynamic test: presents and discusses dynamic results.

- **Section 2.6** Conclusion: generally summarizes the main findings from the research and gives several guidelines for future work.

2.2   Design and fabrication of textured sensors

This section provides a background of textured SEC technology. It also includes a brief description of the fabrication process and electromechanical model. The fabrication process of a pristine SEC, described in details in Laflamme et al. (2013a), was adapted for this study. Figure 2.1 presents the flowchart of the fabrication process of a textured SEC.
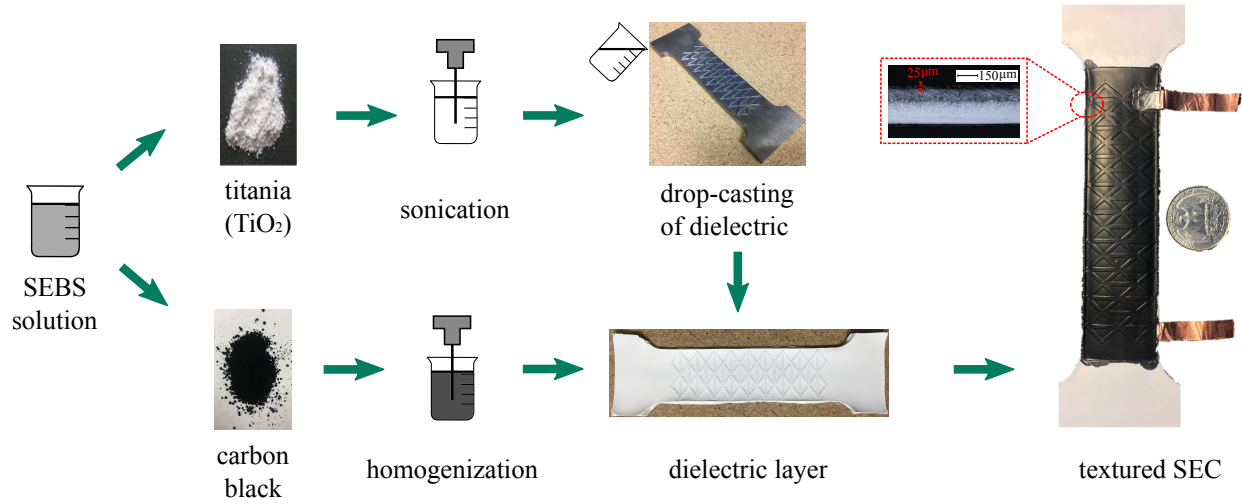
Figure 2.1   Fabrication process of a textured SEC.

2.2.1   Dielectric film

To fabricate the textured dielectric layer, styrene-ethylene-butylene-styrene (SEBS) FG1901G (KRATON, USA, $\rho = 1400$ kg/m^3, 30%w styrene, permittivity 2.4), and SEBS 500120M (VTC Elastoteknik AB, Sweden, $\rho = 930$ kg/m^3, permittivity 2.2) with a weight ratio of 1:3 are dissolved in toluene at 120 g/L. PDMS-coated titania (TPL, Inc., Albuquerque, NM; $TiO_2(-OSI(CH_3)_2-)$ particles are added to the stock solution to have a concentration of 12 vol%. The particles are added to increase both the durability and permittivity of the dielectric layer Stoyanov et al. (2011). A subsequent sonication employs a dismembrator (high intensity ultrasonic processor Vibracell 75041, Sonics & Materials Inc.,USA) for 5 minutes at 120 W and 20 kHz to achieve a stable dispersion of the TiO_2. A volume of 20 ml is drop-casted directly after the solicitation onto a 152 mm x 30 mm non-stick dog-bone steel mold. The molds are made of H13 steel with a HRC48-50 hardness, and their grooves shaped by electrical discharge machining with a maximum depth of 0.35 mm. The mold surfaces have a 1 μm peak-to-valley accuracy, and an average surface roughness of 0.85 μm. The drop-casted solution is left to dry over 24 h for the toluene to evaporate. After, the dry composite film

is gently removed from the mold and left to dry for another 24 h at room temperature. The resulting film has a thickness of 0.3 mm with a textured height of 0.35 mm and a permittivity of 5.56 computed from capacitance measurements.

2.2.2   Conductive film

An electrode stock solution is prepared by dissolving SEBS, SEBS 500050M (VTC Elasoteknik AB, Sweden) in toluene at 380 g/L and adding 15 % vol of carbon black (CB) particles (Orion, Kingwood, TX). For a homogenous dispersion, a low-speed homogenizer is used for 1 hour at 650 RPM. The top and bottom electrodes are brushed onto the dielectric layer with a consecutive drying step for four hours to create uniform conductive layers with a sheet resistance of approximately 2.6 kΩ/sq (Noncontact Eddy Current Sheet Resistance Meter, 20J3, Delcom Instruments, Prescott, WI) and mean thickness of 25 μm. Adhesive copper tape and PELCO conductive carbon glue (TED Pella, INC., USA) is used to provide mechanical and electrical connections to the data acquisition system (DAQ). Figure 2.2 schematizes materials' deformation behaviors for a pristine and a textured SEC under strain.

8
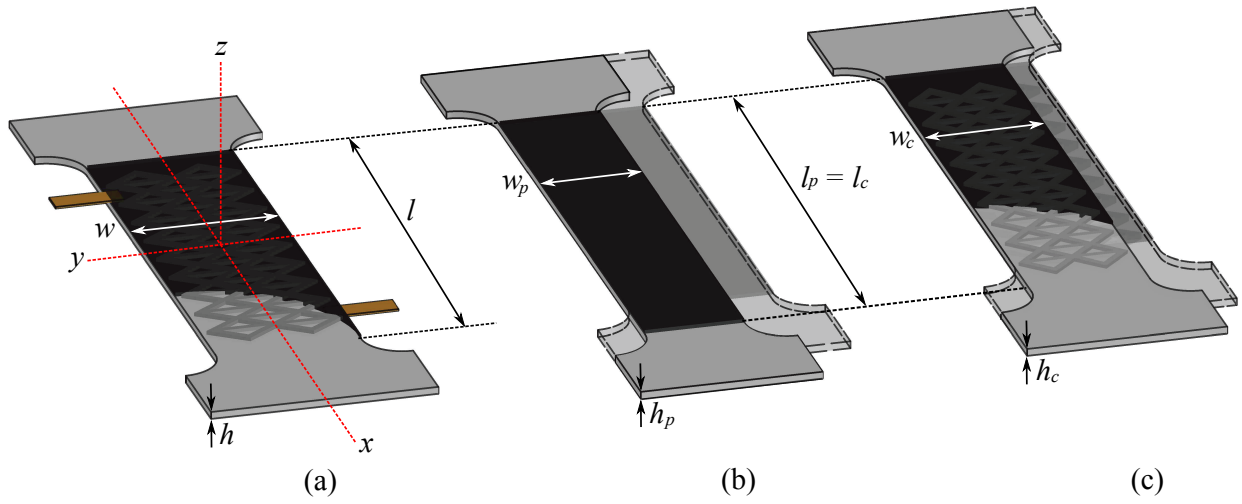
Figure 2.2   (a) Textured sensor in the reference state (under no force) of thickness h and electrode area $l \times w$; (b) pristine SEC in the deformed state (subject to a uniaxial force along x) with altered thickness h_p and electrode area $l_p \times w_p$; and (c) Textured SEC in the deformed state (subject to a uniaxial force along x) with altered thickness h_c and electrode area $l_c \times w_c$.

2.2.3   Electromechanical Model

At low measurement frequency (< 1 kHz), the SEC is modeled as a non-lossy plate capacitor:

$$C = e_0 e_r \frac{A}{h} \tag{2.1}$$

where $e_0 = 8.85$ pF/m is the vacuum permittivity, e_r is relative permittivity of the dielectric, h is the thickness of the dielectric, and $A = w \cdot l$ is the electrode area as annotated in Figure 2.2(a). Assuming small changes in axial strain, differentiating Eq. 2.1 yields an expression relating strain to the relative change in capacitance $\Delta C / C$ with the in-plane strains $\varepsilon_x = \Delta l / l$ and $\varepsilon_y = \Delta w / w$, and out-of-plane strain $\varepsilon_z = \Delta h / h$.

$$\frac{\Delta C}{C} = \left(\frac{\Delta l}{l} + \frac{\Delta w}{w} - \frac{\Delta h}{h} \right)$$
$$= \varepsilon_x + \varepsilon_y - \varepsilon_z \tag{2.2}$$

Taking the SEC as deployed onto a surface along the $x-y$ axes and assuming no pressure along the z axis, one can apply Hooke's law under plane stress assumption with

$$\varepsilon_z = -\frac{\nu}{1-\nu}(\varepsilon_x + \varepsilon_y) \tag{2.3}$$

Similar to the polymer–nanoparticle hybrid dielectrics Zhou et al. (2012), this flexible dielectric is created by incorporating nanoparticles of high dielectric permittivity within the polymer, and the pristine SEC film is isotropic in all directions characterized by the Poisson's ratio ν. Substituting the expression for ε_z from Eq. 2.3 into Eq. 2.2 provides the electromechanical model for the pristine SEC.

$$\frac{\Delta C}{C} = \frac{1}{1-\nu}(\varepsilon_x + \varepsilon_y) \tag{2.4}$$

Textured patterns have stiffness diversity and inhomogeneity of tensile-induced stress distribution on the dielectric layer. Thus, the dielectric layer is treated as orthotropic in the x-y plane. The properties along the sensor differ significantly from those across the sensor governed by the Poisson's ratio ν_{xy}:

$$\nu_{xy} = -\frac{\varepsilon_y}{\varepsilon_x} \tag{2.5}$$

Substituting Eq. 2.5 into Eq. 2.4 yields an electromechanical model for the textured SEC:

$$\frac{\Delta C}{C} = \frac{1-\nu_{xy}}{1-\nu}\varepsilon_x \tag{2.6}$$

where ν is here defined as $\nu = \nu_{xz} = \nu_{yz}$, corresponding to the Poisson's ratio of the pristine SEC. It follows that the gauge factor λ can be expressed as

$$\lambda = \frac{1 - \nu_{xy}}{1 - \nu} \tag{2.7}$$

Eq. 2.7 shows that the capacitance gauge factor solely varies as a function of the Poisson's ratio, which is expected for polymers under axial strain at constant temperature Wen et al. (2008). Assuming ν and ν_{xy} decrease with increasing strain, the gauge factor λ tends to a near-constant value. This will be experimentally verified in Section 4.

2.2.4 Surface Patterns

The surface patterns are created from embossed geometries forming lattices. Geometric discontinuities and varieties are designed to cause inhomogeneous stress distributions, thus altering the Poisson's ratio. Figure 2.3 shows the selected mesh types and layouts. The patterns forming the textures are selected to increase transverse stiffness of the materials, therefore decreasing ν_{xy}. Pattern designs A and C follow a diagrid-like pattern with intersecting diagonal reinforcement Kim and Lee (2010), where Pattern A includes vertical reinforcements. The width of the strips design as 1.4 mm for both Pattern A and B. Among the well-known pattern designs, the diagrid pattern consists of obliquely intersecting diagonal members in lattice form. The triangulated configuration constructed by the diagonal members makes the diagrid structural system can convert the lateral force into axial tension and compression. Thus, it is the most commonly used in high-rise buildings to offer effective lateral rigidity and stiffness. The diagonal elements are angled at 36°, consistent with the optimal angle for a diagrid system in terms of transverse stiffness Moon et al. (2007) (derivation available in Appendix).

Patterns B, E, and F have grid-like arrangements consisting of evenly spaced horizontal and vertical straight lines, and the width of raised strips are design as 1.4 mm for Pattern B and E. Pattern F has fewer vertical reinforcements, but more horizontal reinforcements. Patterns B and E have the same grid arrangement, but with Pattern B constructed using thicker strips, which is 2.5 mm. Pattern D is a grid pattern with curved vertical reinforcement, inspired by the design of metal interconnects in stretchable electronics Lu et al. (2012); Kim et al. (2008) to provide a lateral geometric constraint for tensile-induced transverse shrinkage Gonzalez et al. (2008). Therefore, the straight transverse strips changed as the sinuous arcs with a radius of 8.3 mm and a central angle of $130°$. Pattern G is a pristine pattern which is non-textured taken for benchmarking results. Note that the sequence of patterns is organized following the results from the numerical simulations (presented below), from the lowest to the highest resulting Poisson's ratio ν_{xy}. Comparing with non-textured pristine film, textured surfaces expect to provide both axial and transverse reinforcements for the textured film. The effect of the textured surface has been verify both numerically and experimentally in Chapter 4.
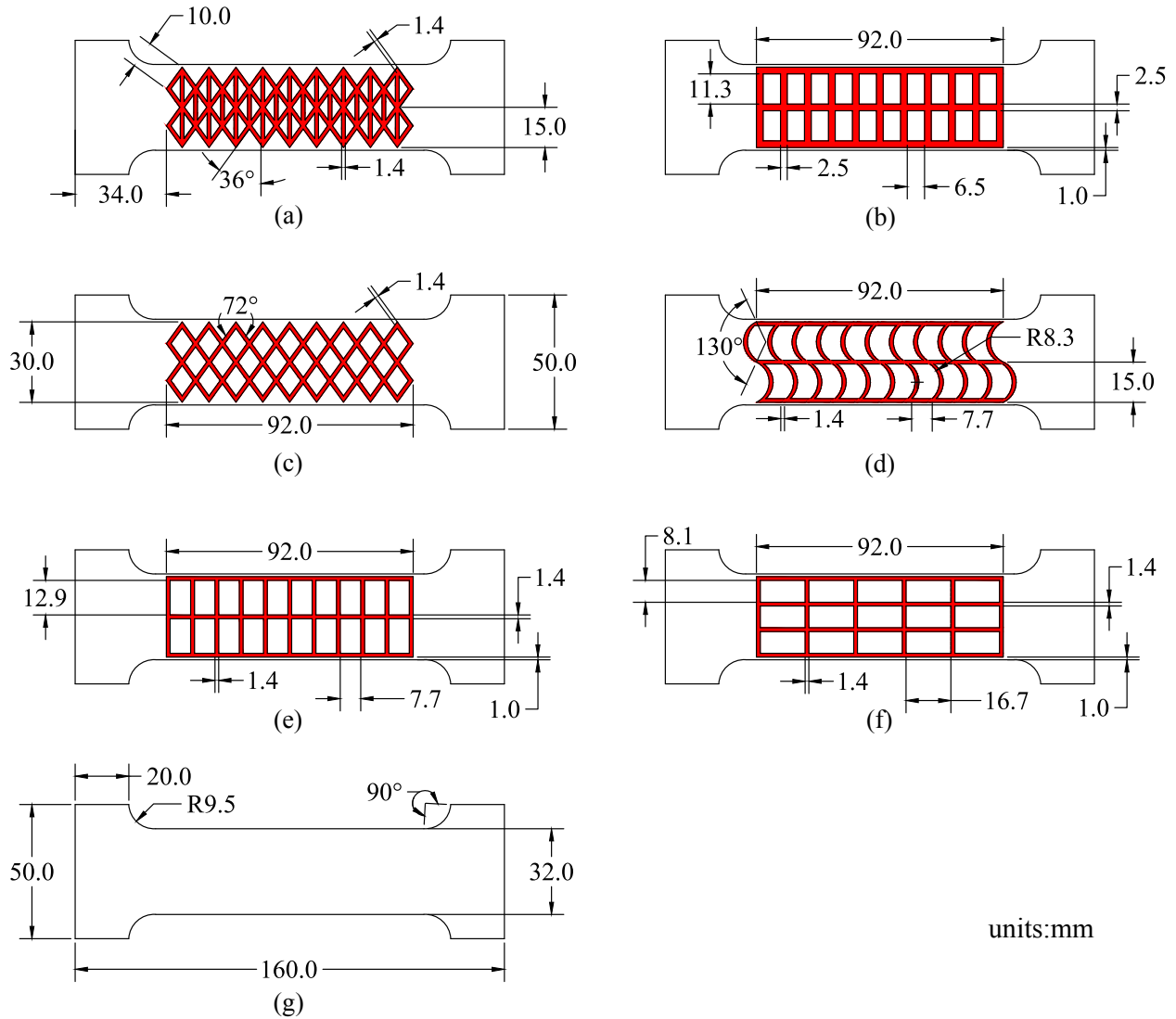
Figure 2.3   Schematics of (a) Pattern A; (b) Pattern B; (c) Pattern C; (d) Pattern D; (e) Pattern E; (f) Pattern F; (g) Pattern G; and (h) section view of mold.

2.3   Methodology

As discussed in the previous section, the performance of the gauge factor relies on the Poisson's ratio, as the decreasing value in ν_{xy} leads to an increase in the gauge factor. Attributes such as linearity and resolution are also dependent on the sensor pattern design. The aspect of geometry must be considered in the current SEC thin film to improve the unidirectional sensing performance. In this section, we first design several patterns, then, finite element modes and experiments performed to investigate the performance the textured SEC.

2.3.1   Numerical Model

Quasi-static nonlinear finite element simulations were conducted in ANSYS 2019 R2 to evaluate the performance of the selected patterns. Three-dimensional FEM models were created by importing the AutoCAD drawings (Figure 2.3) into ANSYS, and material properties were assigned as isotropic with a stiffness of 0.21 MPa experimentally obtained from quasi-static tests on pristine sensors. The Poisson's ratio ν was also obtained experimentally by subjecting pristine SECs to uniaxial strain and measuring deformations using digital image correlation (DIC). For that purpose, two digital cameras (Photron FASTCAM SA-Z) were used to image pristine specimens during the stretching process, which allowed the extraction of transverse strains to compute the apparent Poisson's ratio. Figure 2.4(a) shows the digitally obtained Poisson's ratio on a $52.3 \times 6.31 \times 0.32$ mm^3 non-textured 5:1 aspect ratio dielectric film under 10% strain. The Poisson's ratio under each strain level was taken as the area-wide average of values. Results, plotted in Figure 2.4(b), were fit with the 4-degree polynomial, where ε is strain and ν is Poisson's ratio. Automatic triangular meshes with an element size of 0.2 mm were generated using the tetrahedral method. Boundary conditions

were assigned as simply supported at both ends. Each pattern was simulated by applying 10 % strain along the longitudinal direction using a loading rate of 0.01 mm/s.
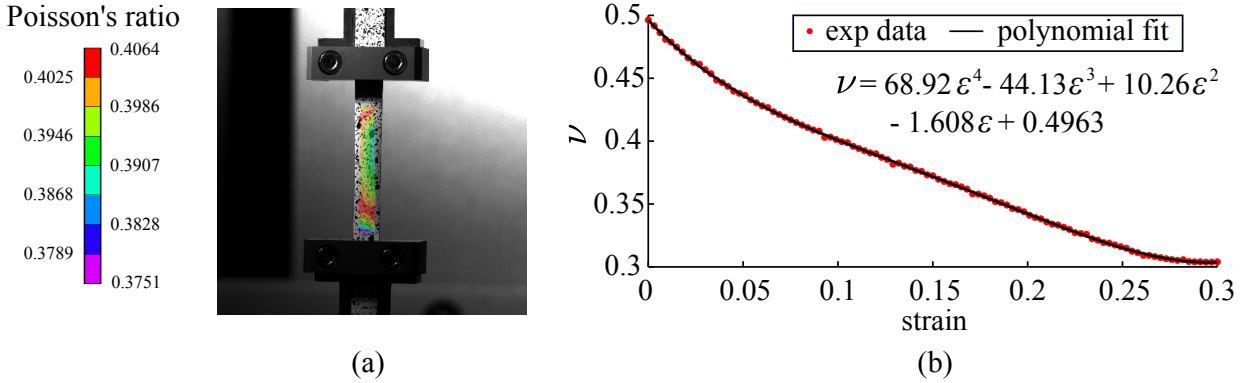
Figure 2.4   (a) Digital image correlation of Poisson's ratio distribution (b) apparent Poisson's ratio for pristine SEC under increasing strain.

2.3.2   Experimental Tests

The specimens (including the pristine specimen) were dog bone-shaped specimens with a total length of 160 mm, gauge length of 111.2 mm, and width of 32 mm (Figure 2.3). The strain experiments were conducted using an Instron 5969 dual column tabletop with ±0.01 mm or 0.05% of displacement measurement accuracy equipped with a 2580 series load cell (shown in Figure 2.5). The passive non-electrode ends of the dog bone specimens were clamped between fiberglass plates adhered to the specimens with an epoxy (JB Weld) and mounted into the tensile tester. Displacements and axial forces were recorded using a Bluehill DAQ with a 12 Hz sampling frequency.

Two specimens were tested under each pattern. Before each test, each specimen was initially pre-strained by 0.5 % at a constant loading rate of 0.1 mm/s. For the quasi-static tests, target strain was applied at a constant rate and then released. This procedure was repeated three times for each sample. For dynamic tests, specimens were subjected to harmonic excitations of varying frequencies under a constant strain amplitude level, and to triangular

excitations of varying strain amplitude levels under a constant frequency. Capacitance measurements were recorded using a LCR meter (Agilent 4263B) with a testing frequency of 1 kHz and sampling frequency of 10 Hz. Signal accuracy through capacitance-strain signal matching and the gauge factor were used as metrics to evaluate the performance of the sensors. Note that DIC was not utilized to obtain the transverse Poisson's ratio directly; instead, it was backtracked through the electromechanical model.
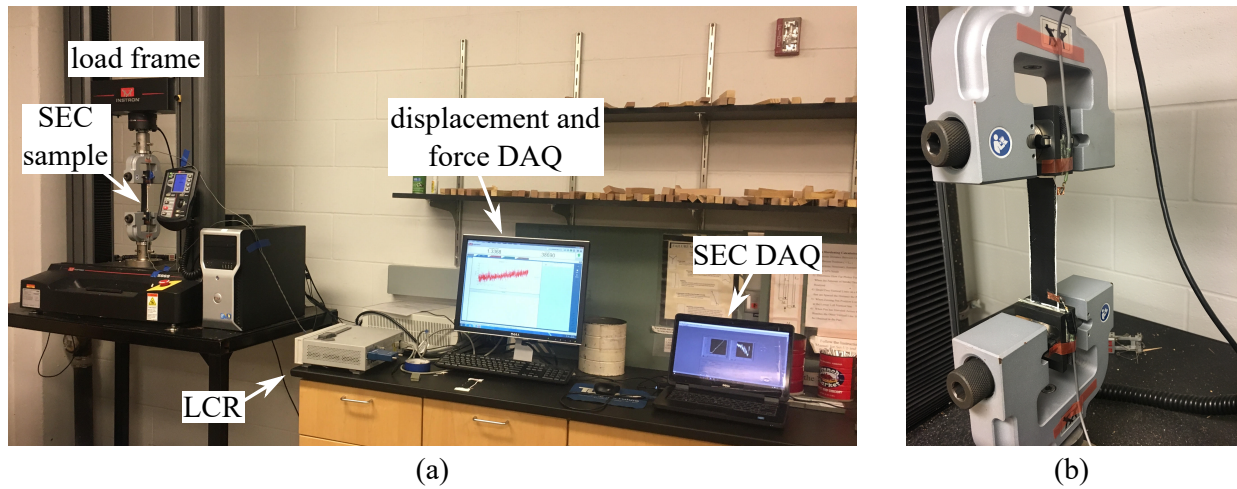
Figure 2.5   The experimental setup consists of a (a) the textured sensor in the dynamic testing machine; and (b) a close-up on the textured sensor.

2.4   Results and Discussion

This section includes the numerical model validation, numerical study, and Quasi-static test. To characterize the sensing electromechanical behaviour of different pattern designs, each textured SEC was investigated under quasi-static tensile test.

2.4.1   Numerical Model Validation

The validation of the numerical model was conducted by matching force-strain curves obtained experimentally on the seven patterns. Figure 2.6 compares the experimental and

numerical axial forces versus strain over 30 % strain under each pattern, where the experimental strain values represent the average of two specimens and numerical values were obtained by simulating the same axial forces (Figure 2.6). The root mean square errors (RSME) of the fit are listed in the bottom right of Figure 2.6. The overall RMSE values range from 0.65 to 1.19 % strain, which indicate a good match between the experimental data and numerical models, therefore validating the accuracy of the numerical model. Discrepancies in results can be attributed to the hand-fabrication process. Results from Figure 2.6 can also be used to study the axial stiffnesses of each pattern. Compared to the pristine SEC (Pattern G), all of the textured sensors exhibit a higher axial stiffness, confirming the effect of axial reinforcements provided by the different patterns.

pattern	A	B	C	D	E	F	G
RMSE (% strain)	0.65	0.62	0.86	0.69	0.57	1.19	1.05
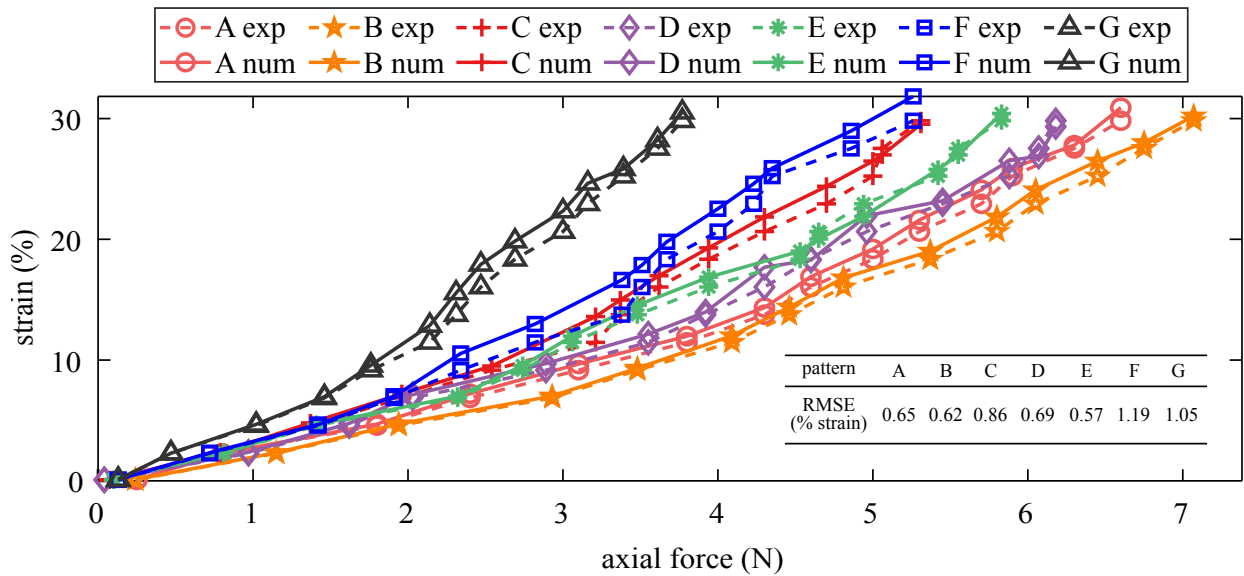
Figure 2.6   Experimental versus numerical strain-force curves for all studied surface pattern.

2.4.2   Numerical Study

The validated numerical model was used to investigate the effects of different texture geometries on the stress distribution. Figure 2.7 presents the normal stress distribution

obtained numerically for each pattern under 10% strain. It can be observed that 1) the overall tensile-induced stresses (positive value) are distributed on the substrate films and longitudinal strips; 2) the compression stresses (negative value) are concentrated in the raised strips along the transverse direction due to the inhomogeneity of the textured configuration; and 3) the existence of transverse (or vertical) strips significantly reduces the magnitude of tensile-induced stresses distributed in the substrate layer.
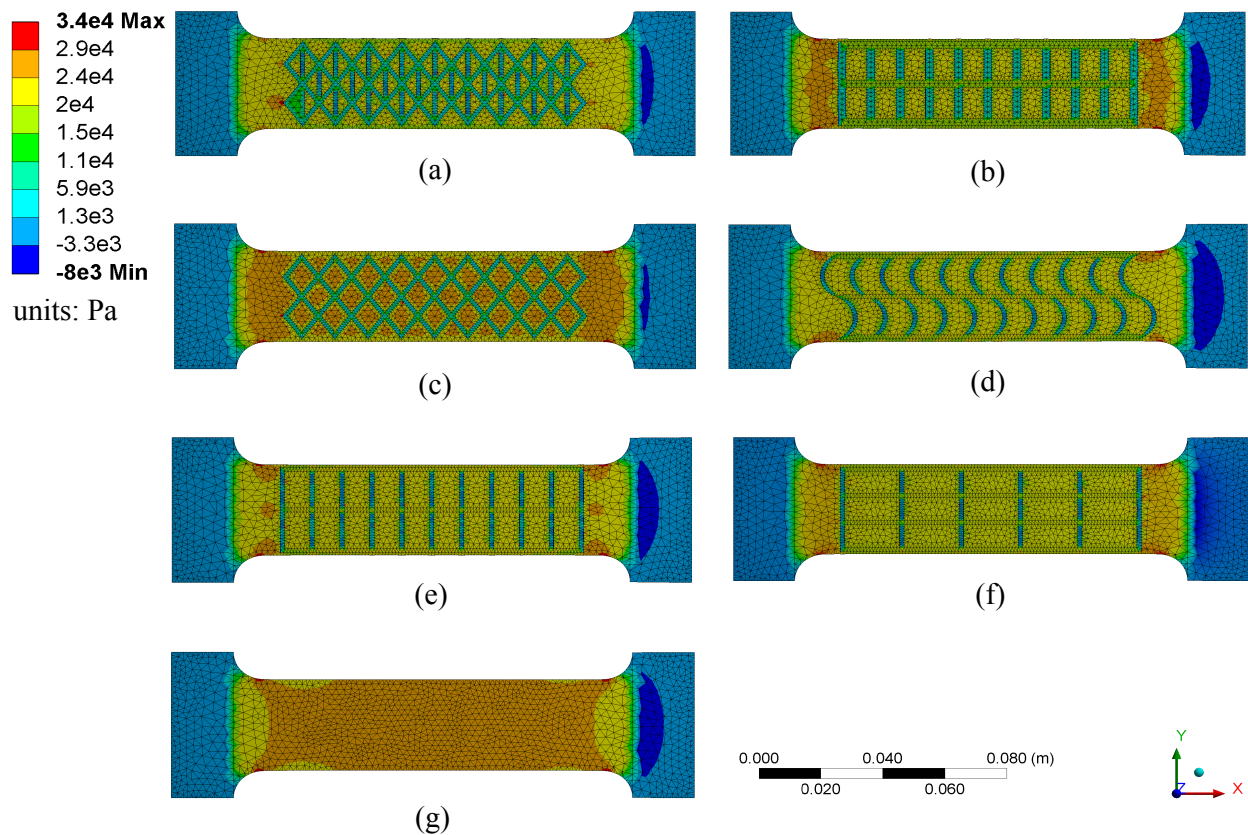
Figure 2.7   Simulated stress distribution for 10% applied strain: (a) Pattern A; (b) Pattern B; (c) Pattern C; (d) Pattern D; (e) Pattern E; and (f) Pattern F; and (g) Pattern G.

After, the transverse Poisson's ratio ν_{xy} was obtained numerically from the resulting transverse shrinkage and known longitudinal elongation under 1%, 5%, 10%, 20%, and 30% longitudinal strain. Figure 2.8 plots the results. The transverse Poisson's ratios increase

from Pattern A to G under all strain levels. It follows that Pattern A is expected to have the highest strain sensitivity and Pattern G the lowest.
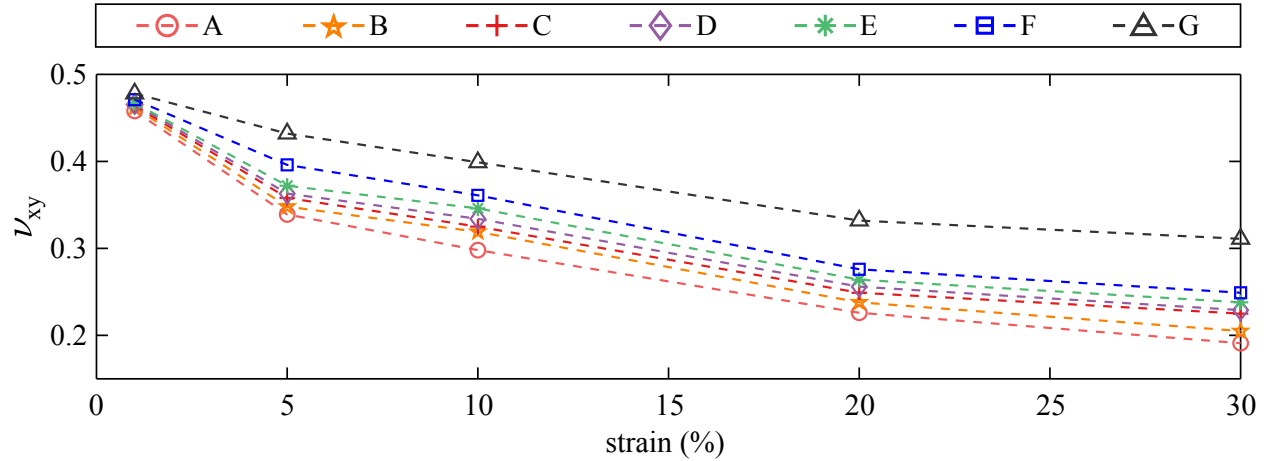
Figure 2.8   Simulated apparent Poisson's ratio for studied pattern under axial strain.

Results also reveal that the stress in the transverse direction is tunable by altering the width and height of the strips to provide additional cross-sectional area, a process known as mechanical stiffening. It is noticed that Patterns B and E, which have the same grid geometry but different strip width, yield two different transverse Poisson's ratios, whereas the use of a larger cross-sectional area results in a lower Poisson's ratio. An enhanced investigation on the effect of strip widths and heights on the apparent Poisson's ratio was conducted using Pattern A. A first set of simulations held the strip width fixed at 1.4 mm, and varied the strip height from 0 to 0.9 mm in 0.05 mm intervals. Results, plotted in Figure 2.9 (black line), indicate that the transverse Poisson's ratio decreases as the strip height increases and converges at approximately 0.8 mm, with a notable gain on ν_{xy} between 0.2 mm and 0.5 mm. A second set of simulations held the strip height constant, but varies the strip width from 0 to 1.8 mm in 0.1 mm intervals. Results, plotted in Figure 2.9 (red line), also shows convergence of the transverse Poisson's ratio, here at approximately 1.5 mm, and an important transition zone, here between 0.4 mm and 1.2 mm. Although results from this investigation conclude

on 0.8 mm being an optimal height, a height of 0.35 mm was selected to ease the fabrication process (from the manual demolding), with a strip width of 1.4 mm.
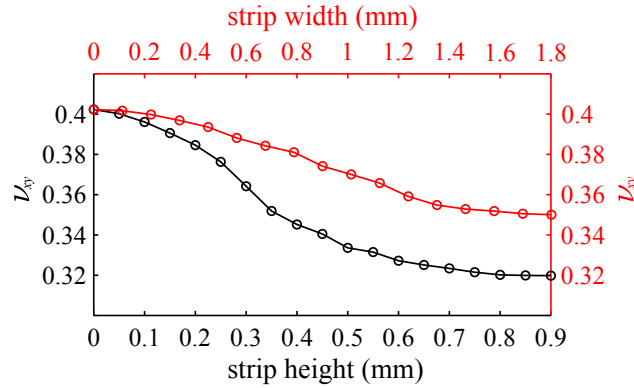
Figure 2.9   Apparent Poisson's ratio of Pattern A under varying strip height and strip width.

2.4.3   Quasi-Static Tests

Quasi-static tests were conducted to investigate the linearity of the sensor under high levels of strain (up to 30 %) applied at a rate of 0.3 mm/s. Figure 2.10(a) plots the relative change in capacitance $\Delta C/C_0$ versus the applied strain, with the solid lines resulting from a linear fit of the experimental data. The overlap of experimental data by the solid lines illustrates the high quality of the linearity of the sensor. This linearity obtained up to 30 % demonstrates a net advantage of the sensor over conventional off-the-shelf strain gauges.
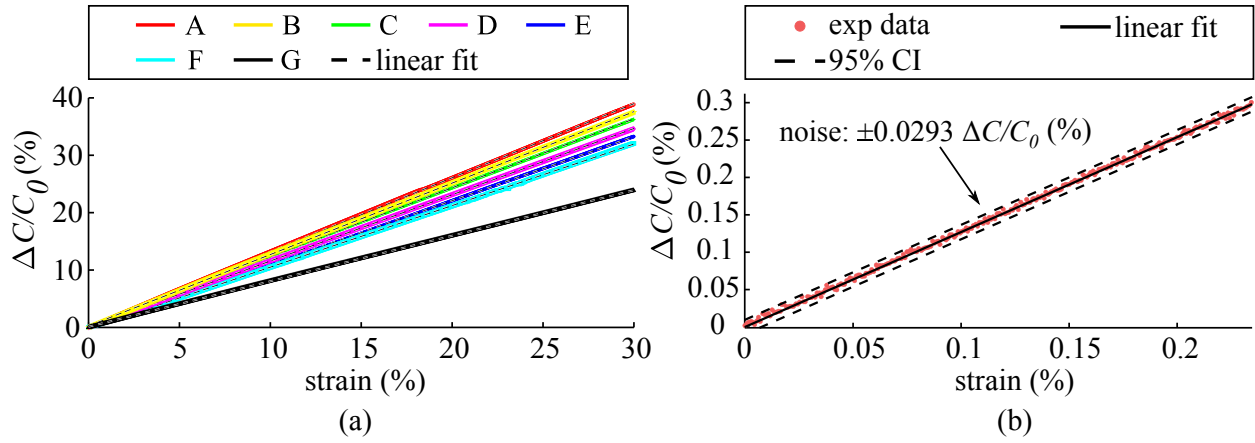
Figure 2.10   (a) Quasi-static tensile test for 30% strain for each pattern (b) capacitance noise of Pattern A with 95% confidence intervals.

Experimentally obtained gauge factors (λ_{exp}) were taken directly from the fitted experimental data (Figure 2.10(a)), and compared against the numerically obtained gauge factors (λ_{num}) taken by substituting the numerically obtained transverse Poisson's ratio into Eq. 2.7. Additional tests were performed at a lower strain rate, $0.01\,\mathrm{mm/s}$, applied up to $5\,\%$, to evaluate the stability of the gauge factor. Results under each pattern are tabulated in Table 2.1. It can be observed that the experimental gauge factors are approximately $2\,\%$ to $9\,\%$ higher than the numerically predicted values, with the discrepancy being generally higher for textures yielding higher gauge factors. These discrepancies may be caused by the manual fabrication process causing unmodeled stress concentrations, in particular for textures of higher complexities such as Patterns A and C. Overall, the ranking of the patterns in terms of gauge factors (or transverse Poisson's ratio) remains the same, with Pattern A exhibiting an improvement of approximately $30\,\%$ in the gauge factor with respect to Pattern G (pristine SEC). Comparing results for different loading rates shows that the gauge factor is stable, with a maximum variation of $0.3\,\%$ found in Pattern G.

Table 2.1 Difference (diff) between experimental gauge factor λ_{exp} and numerical gauge factor λ_{num} as a function of pattern under 0.01 mm/s and 0.3 mm/s loading rates.

Pattern	0.01 mm/s			0.3 mm/s		
	λ_{exp}	λ_{num}	diff (%)	λ_{exp}	λ_{num}	diff (%)
A	1.268	1.164	8.93	1.261	1.157	8.99
B	1.231	1.148	7.23	1.231	1.142	7.79
C	1.220	1.130	7.97	1.217	1.123	8.37
D	1.181	1.121	5.35	1.183	1.117	5.91
E	1.169	1.106	5.70	1.169	1.104	5.89
F	1.116	1.081	3.24	1.108	1.086	2.03
G	0.976	1.000	2.40	0.973	1.000	2.70

Next, the signal matching error over small strain levels was investigated under a strain rate of 0.01 mm/s applied up to 5 % strain. Figure 2.10(b) plots the result under Pattern A, selected because it exhibited the lowest transverse Poisson's ratio, with results zoomed over the 0-0.20% strain region for clarity. The plot also shows the 95% confidence interval (CI) bound $\pm 0.0293\ \Delta C/\ C_0$ (%), equivalent to $\pm 2.29 \mu\varepsilon$ using the electromechanical model (Eq. 2.7) with the gauge factor $\lambda = 1.268$. Comparatively, the 95% CI bound for the pristine SEC (not shown in the plot) is $\pm 0.0345\ \Delta C/\ C_0$ (%), equivalent to $\pm 3.53 \mu\varepsilon$ (Eq. 2.7 with λ=0.976). Pattern A resulted in a 35% improvement in accuracy.

Table 2.2 Experimental gauge factor and 95 % CI accuracy under various loading rates.

Loading rate (mm/s)	λ_{exp}	95% CI	
		$\Delta C/C_0$ (%)	$\mu\varepsilon$
0.0005	1.259	± 0.0341	± 2.708
0.001	1.256	± 0.0334	± 2.659
0.003	1.268	± 0.0325	± 2.563
0.005	1.269	± 0.0306	± 2.411
0.01	1.261	± 0.0298	± 2.363
0.03	1.262	± 0.0272	± 2.155
0.3	1.261	± 0.0193	± 1.531

The effects of the loading rate was further studied for Pattern A using the consequent strain rates of 0.0005 mm/s, 0.001 mm/s, 0.003 mm/s, 0.005 mm/s, 0.01 mm/s, 0.03 mm/s, and 0.3 mm/s to achieve a strain target of 2.5 %. Table 2.2 lists λ_{exp} along with the 95 % CI bound and equivalent strain accuracy using Eq. 2.7 and the associated λ_{exp}. It is evident that the gauge factors are constant for different loading rates, with a maximum difference of 1.04%. However the accuracy of gauge factor decreases with increasing loading rate, which is attributed to the overall mechanical properties of the employed soft composite and the performance of the load cell at low strain rates.

2.5 Dynamic Tests

To further investigate the stability and reversibility of the strain sensing under harmonic excitations, dynamic cyclic tests were are conducted, which include cyclic loading tests with varied frequencies and amplitudes. The setup of tested specimen keeps identical with previous conducted quasi-static test.

2.5.1 Dynamic Tests

Pattern A was selected to conduct tests under dynamic loads, because it exhibited the best performance in terms of gauge factor. Tests consisted of applying a harmonic load of 1.11 mm amplitude (1% strain) of increasing frequency at 0.1, 0.3, 0.5, 0.8, 1.1, and 1.3 Hz, with each of the frequency applied over 10 cycles. Figure 2.11(a) presents a time series plot for Pattern A, compared against the strain input. Good correlations were qualitatively observed between the applied strain (red dashed line) and measured relative capacitance change from SEC (black solid line) of pattern A. Therefore, the sensor is capable of tracking the strain, but with an increasing error with an increasing frequency input, in particular beyond 1 Hz. That phenomenon is possibly due to the strain-rate dependency of the SEBS material and

the softer bonds caused by the adiabatic heating effect, as discussed in a previous study on the dynamic characterization of the SEC technology Laflamme et al. (2015).

Figure 2.11(b) is a plot of the response in the Fourier domain for Pattern A, showing that the frequency response of the sensor can track the frequency content of the input. Here, frequency domain refers to the analysis of signals with respect to frequency. Figure 2.11(b) also presents the extracted gauge factors as a function of the frequency input, representing the frequency response function, for each sensor pattern under investigation. Results show that the gauge factor decreases with increasing frequency, consistent with the findings in previous work on the SEC Saleem et al. (2015), where the dynamic behavior of the gauge factor was modeled up to $40\,\mathrm{Hz}$. The ranking of sensor performance in terms of λ remains consistent throughout each frequency input. Similar results were obtained for other textured SEC with different patterns. The conducted dynamic cyclic tests with varied frequencies validated the good stability and reversibility of the strain sensing of textured SEC. Therefore, textured SEC is promising to serve as a unit element of a capacitance-based sensing skin for SHM application.
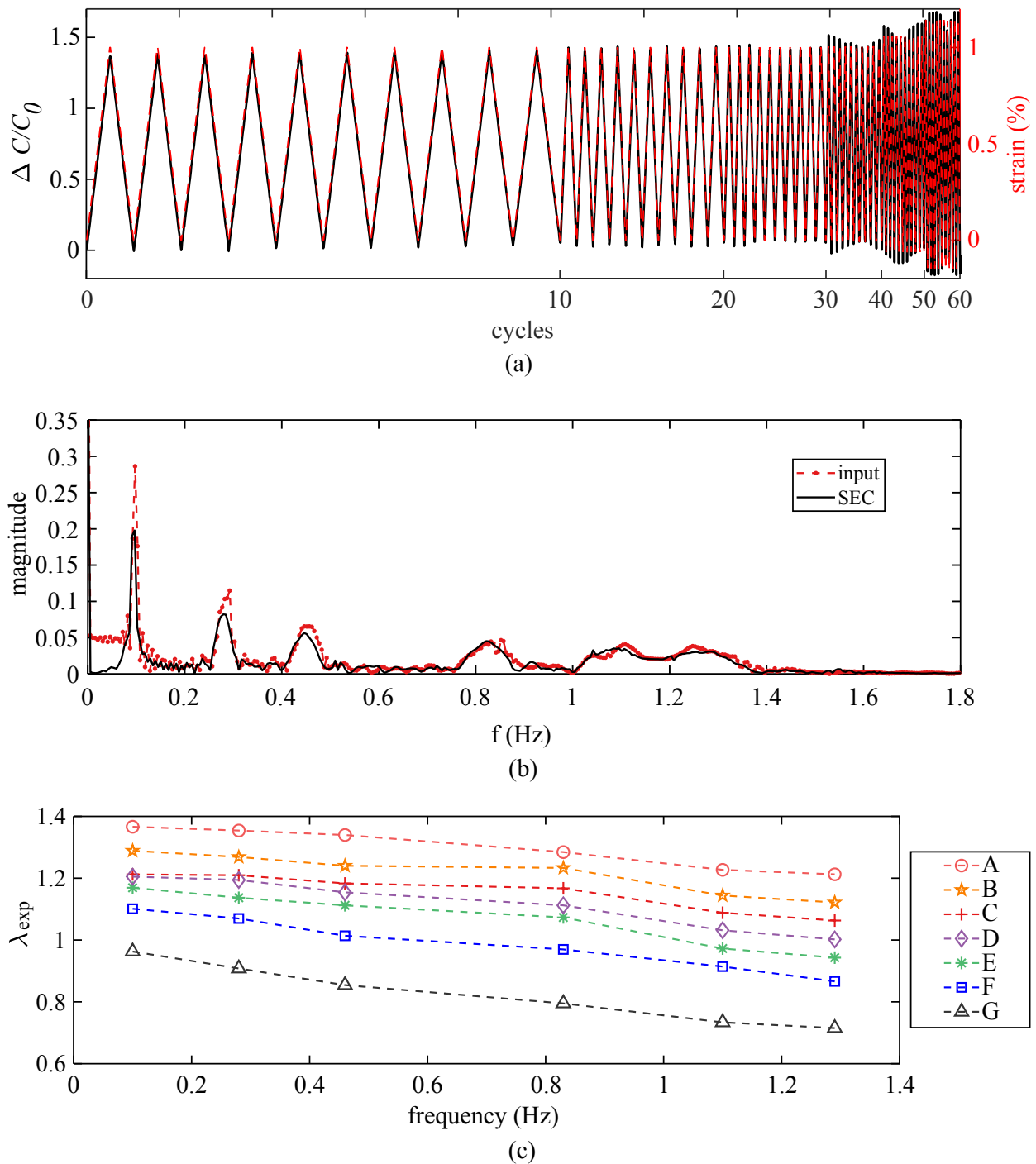
Figure 2.11   (a) Time series response of textured sensor Pattern A under cyclic load-
ing; (b) Frequency response of textured sensor Pattern A; and (c) Plot
of experimental gauge factor as a function of frequency input under each
pattern.

Lastly, the stability of the gauge factors under dynamic loads was evaluated by subjecting the specimens to triangular loads at a constant frequency of $0.3\,\mathrm{Hz}$ of increasing strain amplitude at 0.5, 1, 1.5, 2, 3, 4, and $5\,\%$, with each strain level applied over five cycles. Figure 2.12(a) plots the time series response of Pattern A against the strain input. Results show good agreement, with the error slightly increasing with the increasing strain levels, which may be an intrinsic contribution of the materials composite itself. The experimental gauge factor under each pattern and applied strain amplitude is plotted in Figure 2.12(b). It is worth to notice that the gauge factors remain approximately constant throughout each strain level.
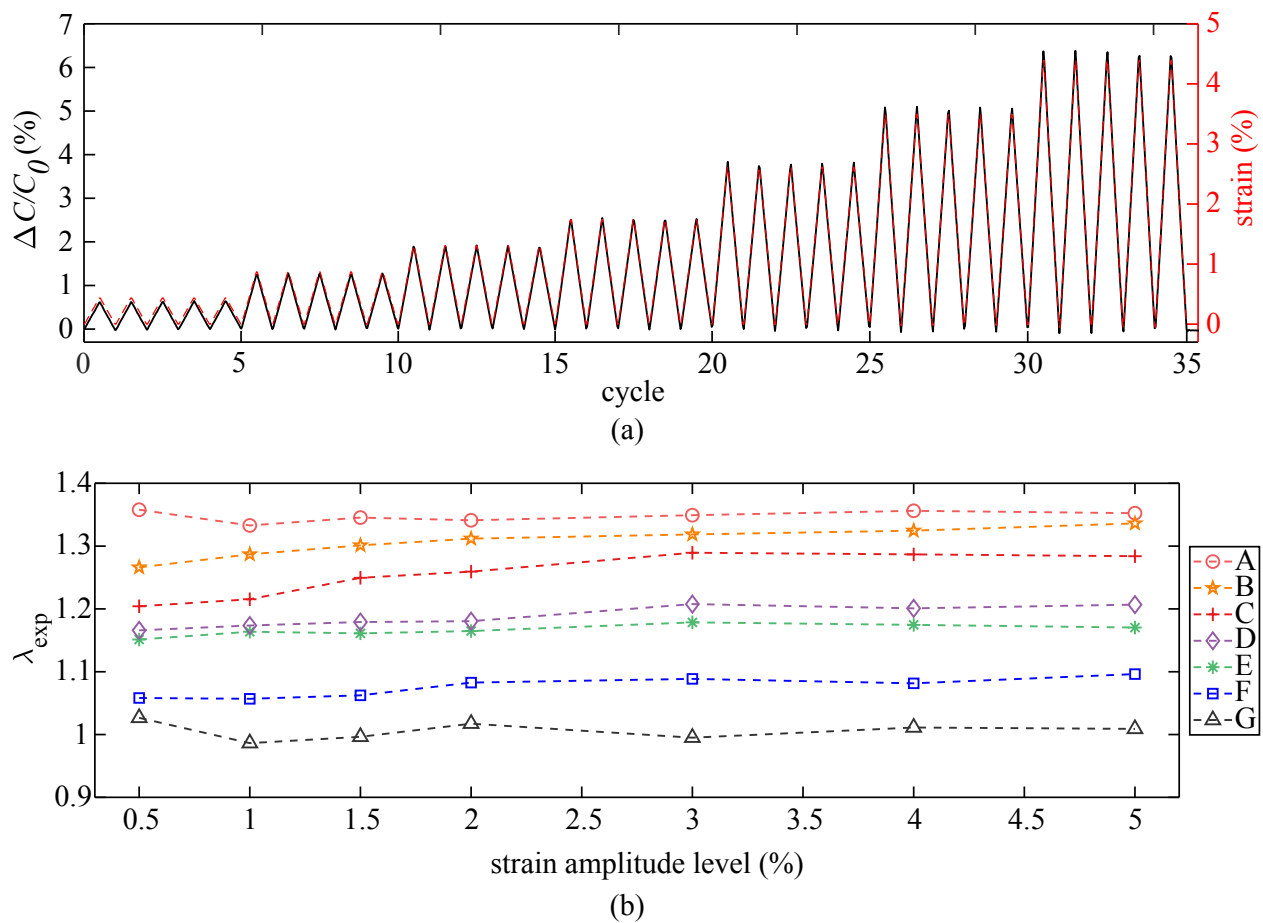

Figure 2.12   (a) Cyclic loading test with varied amplitude; and (b) capacitance gauge factor.

2.6   Conclusion

This paper proposed to texture stretchable capacitive-based strain sensors in order to improve the directionality of measurements. Textures are created by drop-casting an SEBS-composite solution in molds equipped with surface patterns. Six textures were proposed and their performance assessed in terms of reducing the transverse Poisson's ratio, and thus augmenting the gauge factor over uniaxial strain. This was done using both numerically through a validated finite element model, and experimentally by characterizing the electrical signal as a function of quasi-static and dynamic strain inputs. The performance was assessed against that of a pristine sensor, i.e. without texture.

Results from the numerical investigation showed that altering the lattice's geometry, strip heights, and strip widths had a significant effect on the transverse Poisson's ratio. The optimal design was identified as a diagrid with transverse reinforcement vertical strips (Pattern A). Experimental tests confirmed that such geometry yielded an increase of 30 % in the gauge factor compared to the pristine sensor, improvement in signal accuracy of approximately 35%, and maintained linearity of the sensor signal up to 30 % strain. The gauge factor showed nearly constant as a function of strain rate and maximum applied amplitudes, but decreased over increasing loading frequencies.

Overall, the results presented in this paper demonstrated the practicability of textured stretchable capacitive strain sensors with potential application for structural health monitoring. The application of these stretchable sensors in dense networks has the promise to improve strain mapping capabilities for condition assessment applications. It is foreseen that texturing of sensors will become an essential feature of bio-inspired sensing skins due to the ease of fabrication and improve sensing performance, with potential deployments in other fields such as bio-sensing and soft robotics.

References

Burton, A. R., Sun, P., and Lynch, J. P. (2019). Bio-compatible wireless inductive thin-film strain sensor for monitoring the growth and strain response of bone in osseointegrated prostheses. *Structural Health Monitoring*, page 147592171983145.

Chou, C.-P. and Hannaford, B. (1996). Measurement and modeling of McKibben pneumatic artificial muscles. *IEEE Transactions on Robotics and Automation*, 12(1):90–102.

Deimel, R. and Brock, O. (2015). A novel type of compliant and underactuated robotic hand for dexterous grasping. *The International Journal of Robotics Research*, 35(1-3):161–185.

Downey, A., D'Alessandro, A., Ubertini, F., and Laflamme, S. (2018). Automated crack detection in conductive smart-concrete structures using a resistor mesh model. *Measurement Science and Technology*, 29(3):035107.

Downey, A., Laflamme, S., and Ubertini, F. (2016). Reconstruction of in-plane strain maps using hybrid dense sensor network composed of sensing skin. *Measurement Science and Technology*, 27(12):124016.

Downey, A., Laflamme, S., and Ubertini, F. (2017). Experimental wind tunnel study of a smart sensing skin for condition evaluation of a wind turbine blade. *Smart Materials and Structures*, 26(12):125005.

Gonzalez, M., Axisa, F., Bulcke, M. V., Brosteaux, D., Vandevelde, B., and Vanfleteren, J. (2008). Design of metal interconnects for stretchable electronic circuits. *Microelectronics Reliability*, 48(6):825–832.

Gupta, S., Gonzalez, J. G., and Loh, K. J. (2016). Self-sensing concrete enabled by nano-engineered cement-aggregate interfaces. *Structural Health Monitoring*, 16(3):309–323.

Hallaji, M., Seppänen, A., and Pour-Ghaz, M. (2014). Electrical impedance tomography-based sensing skin for quantitative imaging of damage in concrete. *Smart Materials and Structures*, 23(8):085001.

Ilievski, F., Mazzeo, A. D., Shepherd, R. F., Chen, X., and Whitesides, G. M. (2011). Soft robotics for chemists. *Angewandte Chemie International Edition*, 50(8):1890–1895.

Kim, D.-H., Song, J., Choi, W. M., Kim, H.-S., Kim, R.-H., Liu, Z., Huang, Y. Y., Hwang, K.-C., w. Zhang, Y., and Rogers, J. A. (2008). Materials and noncoplanar mesh designs for integrated circuits with linear elastic responses to extreme mechanical deformations. *Proceedings of the National Academy of Sciences*, 105(48):18675–18680.

Kim, J. and Lee, Y.-H. (2010). Seismic performance evaluation of diagrid system buildings. *The Structural Design of Tall and Special Buildings*, 21(10):736–749.

Kollosche, M., Stoyanov, H., Laflamme, S., and Kofod, G. (2011). Strongly enhanced sensitivity in elastic capacitive strain sensors. *Journal of Materials Chemistry*, 21(23):8292.

Kong, X., Li, J., Bennett, C., Collins, W., and Laflamme, S. (2016). Numerical simulation and experimental validation of a large-area capacitive strain sensor for fatigue crack monitoring. *Measurement Science and Technology*, 27(12):124009.

Laflamme, S., Kollosche, M., Connor, J. J., and Kofod, G. (2013a). Robust flexible capacitive surface sensor for structural health monitoring applications. *Journal of Engineering Mechanics*, 139(7):879–885.

Laflamme, S., Saleem, H. S., Vasan, B. K., Geiger, R. L., Chen, D., Kessler, M. R., and Rajan, K. (2013b). Soft elastomeric capacitor network for strain sensing over large surfaces. *IEEE/ASME Transactions on Mechatronics*, 18(6):1647–1654.

Laflamme, S. and Ubertini, F. (2019). Back-to-basics: Self-sensing materials for nondestructive evaluation. *Materials Evaluation*.

Laflamme, S., Ubertini, F., Saleem, H., D'Alessandro, A., Downey, A., Ceylan, H., and Materazzi, A. L. (2015). Dynamic characterization of a soft elastomeric capacitor for structural health monitoring. *Journal of Structural Engineering*, 141(8):04014186.

Lee, B. M., Gupta, S., Loh, K. J., and Nagarajaiah, S. (2016). Strain sensing and structural health monitoring using nanofilms and nanocomposites. *Innovative Developments of Advanced Multifunctional Nanocomposites in Civil and Structural Engineering*, pages 303–326. Elsevier.

Li, Y., Luo, S., Yang, M.-C., Liang, R., and Zeng, C. (2016). Poisson ratio and piezoresistive sensing: A new route to high-performance 3d flexible and stretchable sensors of multimodal sensing capability. *Advanced Functional Materials*, 26(17):2900–2908.

Liao, X., Liao, Q., Yan, X., Liang, Q., Si, H., Li, M., Wu, H., Cao, S., and Zhang, Y. (2015). Flexible and highly sensitive strain sensors fabricated by pencil drawn for wearable monitor. *Advanced Functional Materials*, 25(16):2395–2401.

Liu, H., Yan, J., Kollosche, M., Bentil, S., and Laflamme, S. (2020). Surface textures for stretchable capacitive strain sensors. *Smart Materials and Structures-IOPscience*.

Lu, N., Lu, C., Yang, S., and Rogers, J. (2012). Highly sensitive skin-mountable strain gauges based entirely on elastomers. *Advanced Functional Materials*, 22(19):4044–4050.

Manna, K., Wang, L., Loh, K. J., and Chiang, W.-H. (2019). Printed strain sensors using graphene nanosheets prepared by water-assisted liquid phase exfoliation. *Advanced Materials Interfaces*, 6(9):1900034.

Martinez, R. V., Fish, C. R., Chen, X., and Whitesides, G. M. (2012). Elastomeric origami: Programmable paper-elastomer composites as pneumatic actuators. *Advanced Functional Materials*, 22(7):1376–1384.

Mohammad, I. and Huang, H. (2010). Monitoring fatigue crack growth and opening using antenna sensors. *Smart Materials and Structures*, 19(5):055023.

Moon, K.-S., Connor, J. J., and Fernandez, J. E. (2007). Diagrid structural systems for tall buildings: characteristics and methodology for preliminary design. *The Structural Design of Tall and Special Buildings*, 16(2):205–230.

Rogers, J. A., Someya, T., and Huang, Y. (2010). Materials and mechanics for stretchable electronics. *Science*, 327(5973):1603–1607.

Saleem, H., Downey, A., Laflamme, S., Kollosche, M., and Ubertini4, F. (2015). Investigation of dynamic properties of a novel capacitive-based sensing skin for nondestructive evaluation. *Materials Evaluation*.

Shepherd, R. F., Ilievski, F., Choi, W., Morin, S. A., Stokes, A. A., Mazzeo, A. D., Chen, X., Wang, M., and Whitesides, G. M. (2011). Multigait soft robot. *Proceedings of the National Academy of Sciences*, 108(51):20400–20403.

Shintake, J., Nagai, T., and Ogishima, K. (2019). Sensitivity improvement of highly stretchable capacitive strain sensors by hierarchical auxetic structures. *Frontiers in Robotics and AI*, 6.

Srivastava, R. K., Vemuru, V. S. M., Zeng, Y., Vajtai, R., Nagarajaiah, S., Ajayan, P. M., and Srivastava, A. (2011). The strain sensing and thermal–mechanical behavior of flexible multi-walled carbon nanotube/polystyrene composite films. *Carbon*, 49(12):3928–3936.

Stoyanov, H., Kollosche, M., Risse, S., McCarthy, D. N., and Kofod, G. (2011). Elastic block copolymer nanocomposites with controlled interfacial interactions for artificial muscles with direct voltage control. *Soft Matter*, 7(1):194–202.

Tolley, M. T., Shepherd, R. F., Mosadegh, B., Galloway, K. C., Wehner, M., Karpelson, M., Wood, R. J., and Whitesides, G. M. (2014). A resilient, untethered soft robot. *Soft Robotics*, 1(3):213–223.

Tung, S.-T., Yao, Y., and Glisic, B. (2014). Sensing sheet: the sensitivity of thin-film full-bridge strain sensors for crack detection and characterization. *Measurement Science and Technology*, 25(7):075602.

Tybrandt, K., Khodagholy, D., Dielacher, B., Stauffer, F., Renz, A. F., Buzsáki, G., and Vörös, J. (2018). High-density stretchable electrode grids for chronic neural recording. *Advanced Materials*, 30(15):1706520.

Wang, S., Xu, J., Wang, W., Wang, G.-J. N., Rastak, R., Molina-Lopez, F., Chung, J. W., Niu, S., Feig, V. R., Lopez, J., Lei, T., Kwon, S.-K., Kim, Y., Foudeh, A. M., Ehrlich, A., Gasperini, A., Yun, Y., Murmann, B., Tok, J. B.-H., and Bao, Z. (2018). Skin electronics from scalable fabrication of an intrinsically stretchable transistor array. *Nature*, 555(7694):83–88.

Wen, Q., Zhu, J., Gong, S., Huang, J., Gu, H., and Zhao, P. (2008). Design and synthesis of a packaging polymer enhancing the sensitivity of fiber grating pressure sensor. *Progress in Natural Science*, 18(2):197–200.

Yan, J., Downey, A., Chen, A., Laflamme, S., and Hassan, S. (2019). Capacitance-based sensor with layered carbon-fiber reinforced polymer and titania-filled epoxy. *Composite Structures*, 227:111247.

Zhang, B., Wang, S., Li, X., Zhang, X., Yang, G., and Qiu, M. (2014). Crack width monitoring of concrete structures based on smart film. *Smart Materials and Structures*, 23(4):045031.

Zhou, Y., Han, S.-T., Xu, Z.-X., and Roy, V. A. L. (2012). Polymer–nanoparticle hybrid dielectrics for flexible transistors and inverters. *Journal of Materials Chemistry*, 22(9):4060.

Zhou, Z., Zhang, B., Xia, K., Li, X., Yan, G., and Zhang, K. (2010). Smart film for crack monitoring of concrete bridges. *Structural Health Monitoring: An International Journal*, 10(3):275–289.

CHAPTER 3. GENERAL CONCLUSION

This paper presented a study on the potential texturing a soft elastomeric capacitor (SEC) with the textured surface in order to improve the sensing directionality and sensitivity. Both Numerical simulation and experiments have demonstrated the practicability of textured stretchable capacitive strain sensors with potential application for structural health monitoring. The sensor technology is expected to be arranged in a dense network configuration to serve as sensing skin, which provides unprecedented coverage and resolution in terms of state measurement capabilities.

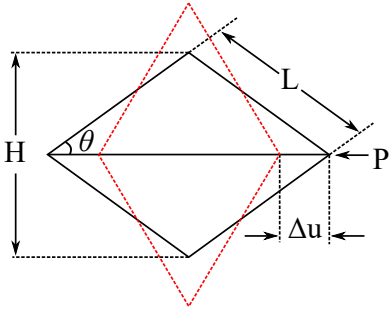# APPENDIX .   ADDITIONAL MATERIAL

A.1   Angle Optimization

Figure A.1   Pattern A schematic plot.

The transverse stiffness k of patter A can be expressed as

$$k = 2\frac{AE}{L}\cos^2\theta = 2\frac{AE}{H}\cos^2\theta\sin\theta \tag{A.1}$$

where A is the cross section area of strips, and E is Young's modulus of the material. The Δu is the resulting transverse displacement when lateral force P is applied

$$P = k\Delta u = 2AE\gamma\cos^2\theta\sin\theta \tag{A.2}$$

take derivative of stiffness k with diagrid angle θ to show stiffness derivation

$$\frac{dk}{d\theta} = 2AE\gamma(\cos^3\theta - 2\cos\theta\sin^2\theta) \tag{A.3}$$

where $\gamma = \Delta u H^{-1}$, to optimaize the diagirds angle θ, minimize the value of Eq.A.3 by assuming

$$\cos^3\theta - 2\cos\theta\sin^2\theta = 0 \tag{A.4}$$

θ can be solved

$$\theta = 35.26° \qquad\qquad\qquad (A.5)$$